Energy Storage Materials 55 (2023) 193–204

Contents lists available at ScienceDirect

Energy Storage Materials

journal homepage: www.elsevier.com/locate/ensm

Synergistic halide-sulfide hybrid solid electrolytes for Ni-rich cathodes design guided by digital twin for all-solid-State Li batteries

Jong Seok Kim [a,1], Seungwon Jung [b,1], Hiram Kwak [a], Yoonjae Han [a], Suhwan Kim [b], Jongwoo Lim [c], Yong Min Lee [b,*], Yoon Seok Jung [a]

[a] Department of Chemical and Biomolecular Engineering, Yonsei University, Seoul 03722, Republic of Korea
[b] Department of Energy Science and Engineering, Daegu Gyeongbuk Institute of Science and Technology (DGIST), Daegu 42988, Republic of Korea
[c] Department of Chemistry, Seoul National University, Seoul 08826, Republic of Korea

ARTICLE INFO

Keywords:
All-solid-state lithium batteries
Halide solid electrolytes
Sulfide solid electrolytes
Digital twins
Electrochemical stabilities

ABSTRACT

Halide solid electrolytes are a promising candidate for all-solid-state Li batteries (ASLBs) owing to their mechanical sintering ability and excellent (electro)chemical oxidation stability. However, these advantages are counteracted by the lower Li^+ conductivities and higher specific densities compared with those of sulfides. Herein, a novel halide-sulfide hybrid catholyte design for Ni-rich layered oxide cathodes for ASLBs is reported. In a hybrid catholyte, Li_3YCl_6 (0.40 mS cm^{-1}) coatings protect the surface of $Li[Ni_{0.88}Co_{0.11}Al_{0.01}]O_2$ while Li_6PS_5Cl (1.80 mS cm^{-1}) serves as a Li^+ highway. $Li[Ni_{0.88}Co_{0.11}Al_{0.01}]O_2$ cathodes with an optimal fraction of Li_3YCl_6, 10 wt% with respect to Li $[Ni_{0.88}Co_{0.11}Al_{0.01}]O_2$, substantially outperform electrodes using either Li_6PS_5Cl or Li_3YCl_6 in terms of capacity (202 vs. 171 or 191 mA h g^{-1} at 0.1C, respectively), initial Coulombic efficiency, rate capability, and cycling performance. The superiority of Li_3YCl_6 for interfacial stability in the Li_3YCl_6-coated electrode to the electrode without Li_3YCl_6 is confirmed by complementary analysis. Moreover, the digital twin model is successfully established and reveals electrically isolated $Li[Ni_{0.88}Co_{0.11}Al_{0.01}]O_2$ particles when 14 wt% Li_3YCl_6 is used. This insight leads to the development of a mixed conductor coating consisting of Li_3YCl_6 and carbon, further enhancing the performance: e.g., 134 vs. 53 mA h g^{-1} at 2C.

1. Introduction

Owing to their safety and high energy density potential, all-solid-state Li batteries (ASLBs) using inorganic solid electrolytes (SEs) are at the heart of extensive research and development for large-scale energy storage applications such as electric vehicles. [1–12] For the development of ASLBs operating at ambient temperature, high ionic conductivity of SEs, at least ~1 mS cm^{-1}, is required. [3–5,7,13,14] In addition, high mechanical deformability of SEs is highly desirable because it allows for the fabrication of ASLBs by a simple cold-pressing process. [5,9,15]

Sulfide SEs, such as argyrodites, $Li_{6-x}PS_{5-x}Cl_{1+x}$ (maximum Li^+ conductivity of ~10 mS cm^{-1}), are the state-of-the-art candidates that satisfy the two major criteria described above. [5,16–19] However, their intrinsic electrochemical oxidation stability is poor; the onset potential for oxidation is < 3 V (vs. Li/Li^+). [5,20,21] Moreover, experimental and theoretical investigations revealed that sulfide SEs are reactive with layered oxide cathode active materials (CAMs) $LiMO_2$ (M = Ni, Co, Mn, and Al mixture), [22–31] and the reactivity becomes more severe for delithiated (or charged) CAMs. [30,31] Owing to these low electrochemical stability and chemical incompatibility, unprotected $LiMO_2$ cathodes combined with sulfide SEs exhibit poor electrochemical performances. [26–32] Therefore, it is a common practice to apply protective oxide coatings on $LiMO_2$, such as $LiNbO_3$, Li_2ZrO_3, and $Li_{3-x}B_{1-x}C_xO_3$. [4,9,33–35] However, an optimal performance might be limited by the low Li^+ conductivities of oxide coating materials (max. ~10^{-6} S cm^{-1}). [33,36] A precise control of their conformality with the thickness of less than tens of nanometer is needed, for which elaborate wet-chemical methods are usually employed. [4,33–35,37]

Halide SEs are another promising SE candidate that meets the requirements of the high ionic conductivity of ≥ 1 mS cm^{-1} and deformability that allows for the mechanical sintering. [32,38–46] Importantly, the Fermi level of chloride bands is much lower than those of sulfide bands, indicating a significantly higher electrochemical

* Corresponding authors.
E-mail addresses: yongmin.lee@dgist.ac.kr (Y.M. Lee), yoonsjung@yonsei.ac.kr (Y.S. Jung).
[1] These authors contributed equally.

https://doi.org/10.1016/j.ensm.2022.11.038
Received 2 October 2022; Received in revised form 17 November 2022; Accepted 20 November 2022
Available online 21 November 2022

oxidation stability of chloride SEs compared with that of sulfide SEs. [47] In 2018, Asano et al. reported an outstanding electrochemical performance of uncoated $LiCoO_2$ using Li_3YCl_6 (LYC), which was attributed to the excellent (electro)chemical stability of LYC. [32] The following extensive efforts identified several novel halide compounds, including Li_3InCl_6 (1.5 mS cm^{-1}), [39] Li_3ScCl_6 (3 mS cm^{-1}), [40,41] and Li_2ZrCl_6 (0.4 mS cm^{-1}). [43] Aliovalent substitutions could further improve the ionic conductivities, e.g., $Li_{3-x}Y_{1-x}Zr_xCl_6$ (1.4 mS cm^{-1}), [48] $Li_{3-x}Yb_{1-x}Hf_xCl_6$ (1.5 mS cm^{-1}), [44] $Li_{2+x}Zr_{1-x}Fe_xCl_6$ (0.98 mS cm^{-1}), [43] and $Li_{2+x}Zr_{1-x}In_xCl_6$ (2.1 mS cm^{-1}). [45] Despite these progresses, the ionic conductivities of halide SEs with max. ~1 mS cm^{-1} have remained lower compared to sulfide SEs. Moreover, halide SEs are heavier than sulfide SEs (e.g., LYC: 2.43 g cm^{-3}, Li_3InCl_6: 2.71 g cm^{-3} vs. $Li_{5.5}PS_{4.5}Cl_{1.5}$: 1.88 g cm^{-3}), which is translated into the lower specific energy density of resulting ASLBs. [31] Moreover, the practical applications of halide SEs suffer from the use of costly central metal elements, mostly rare earth metals, with the exception of Zr. [38,43,49] Overall, the advantage of halide SEs over sulfide SEs, i.e., the excellent

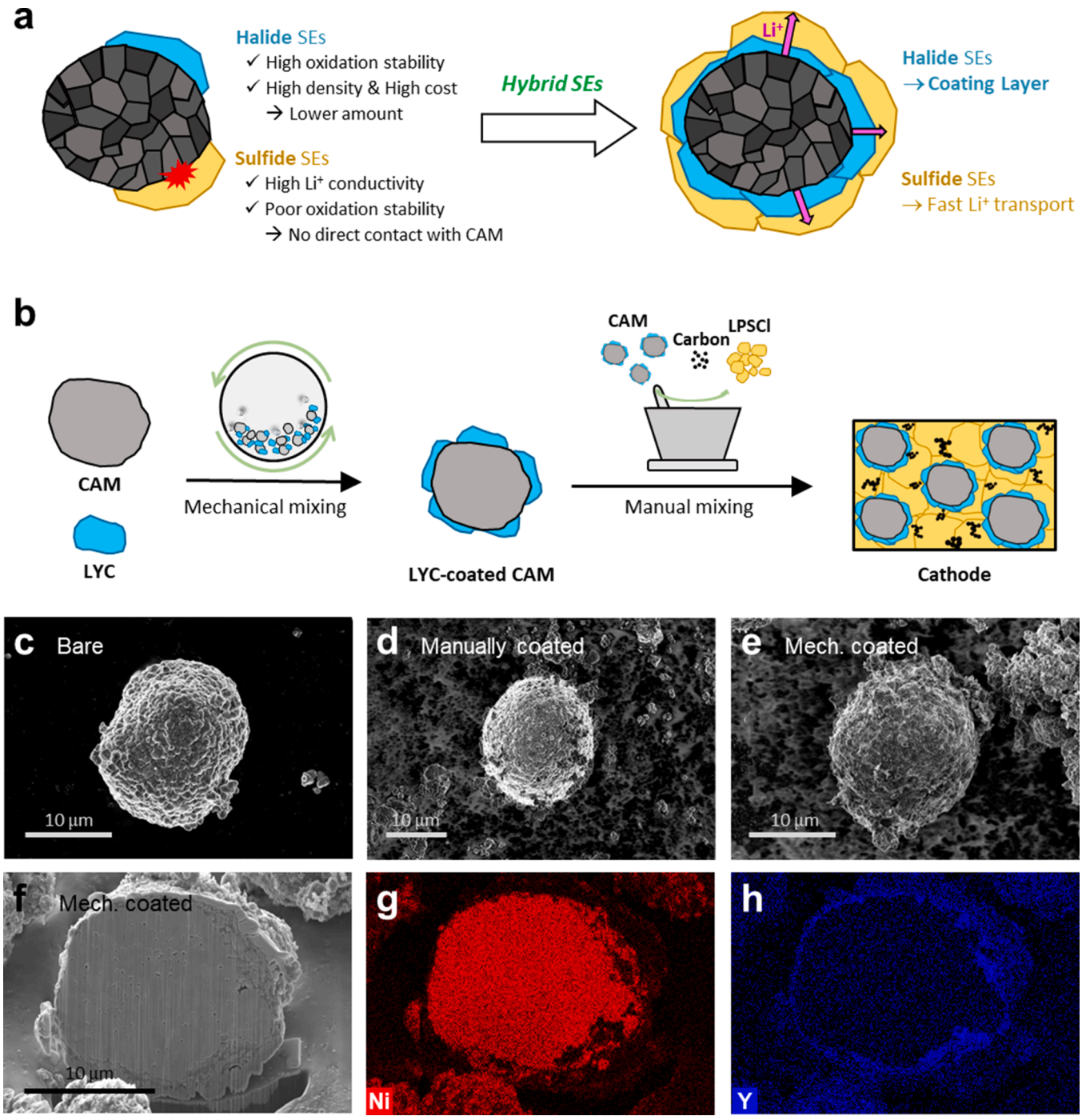

Fig. 1. Design of halide-sulfide hybrid catholytes for Ni-rich-layered oxide cathodes $Li[Ni_{0.88}Co_{0.11}Al_{0.01}]O_2$ (NCA). a) Schematic illustrating pros and cons of halide and sulfide SEs and corresponding design of halide-sulfide catholyte for all-solid-state Ni-rich layered cathodes, wherein the Ni-rich layered CAMs are coated with halide SEs. b) Schematic of the fabrication of NCA cathodes using LYC-LPSCl catholyte. SEM images of c) bare NCA particle, and NCA particles coated with 10 wt% LYC by d) manual and e) mechanical methods. f) Cross-sectional SEM image of NCA particles coated with 10 wt% LYC, prepared by mechanical mixing, and its corresponding EDXS maps for g) Ni and h) Y.

(electro)chemical oxidation stability, is counterbalanced by the lower ionic conductivities, heaviness, and higher costs.

For the development of high-performance electrodes for conventional Li-ion batteries using liquid electrolytes, most studies focused on electrical wiring of electrode active materials. [50,51] The design of composite electrodes in ASLBs is made more complicated by the particulate feature of inorganic SEs. [1,5,23,27,52] SEs and CAMs form defective two-dimensional (2D) ionic contacts. [15,23,31] In addition, unbalanced amounts of SEs and conductive carbon additives often result in the disruption of either electronic or ionic conduction pathways, which leads to below par electrochemical performances of ASLB cells. [53,54] Furthermore, the particle size of SEs could remarkably affect the utilization of CAMs. [31,55,56] Han et al., also showed that the use of CAMs with small particle sizes caused their poor spatial distribution, which resulted in electrochemo-mechanical degradation. [31] Recently, a computational modeling approach emerged as a tool to examine the above complicating factors in micro-structured ASLB electrodes. [57–60] Park et al., adapted digital twin to design ASLB cathodes in which several critical factors were identified, such as dead particles, specific contact area, effective electronic/ionic conductivities, and charge distribution inside cathodes. [58] In addition, Bielefeld et al., evaluated the effective ionic conductivity and tortuosity by a flux-based simulation, and examined the effects of electrode composition on the electrochemical performances. [59]

Based on the aforementioned background and motivations, this study investigates a rational design of halide-sulfide hybrid catholytes. Although halide and sulfide SEs were used as the catholyte and separating SE layer, respectively, in previous reports, [31,38,43–45,49] a hybrid catholyte design has been unprecedented. For the hybrid catholytes in this study, a minimal amount of LYC (0.40 mS cm^{-1}) as a model halide SE coats $Li[Ni_{0.88}Co_{0.11}Al_{0.01}]O_2$ (NCA) CAMs while the sulfide SE, Li_6PS_5Cl (LPSCl), serves as a highway for fast Li^+ transport (1.8 mS cm^{-1}), as is illustrated in Fig. 1a. By this synergistic strategy, NCA electrodes coated with 10 wt% LYC with respect to NCA (or 33 wt% LPSCl with respect to NCA) exhibited an optimal performance; for example, the capacity retention at 2C with respect to the capacity at 0.1C was improved from 16% and 54% for using solely either LPSCl or LYC, respectively, to 61% for using 10 wt% LYC. The LYC coating minimized the direct contacts between NCA and LPSCl and thereby suppressed the degradation, which was validated by complementary analysis using electrochemical impedance spectroscopy (EIS), in situ X-ray diffraction (XRD), ex situ transmission electron microscopy (TEM), and ex situ X-ray photoelectron spectroscopy (XPS) measurements. Furthermore, digital twin modeling established for the NCA electrodes revealed overlooked insufficient electronic conduction pathways of the LYC-coated NCA electrodes, thus further boosting the electrochemical performance through coating a mixed-conducting phase comprising LYC and carbon on NCA particles.

2. Results and discussion

The fabrication of NCA cathodes using a LYC-LPSCl hybrid catholyte proceeded by two steps, as illustrated in Fig. 1b. First, LYC was dry-coated on NCA by mechanical mixing using ball milling. Subsequently, the LYC-coated NCA particles were manually mixed with LPSCl and conductive carbon additives, yielding cathode mixtures. Scanning electron microscopy (SEM) images of bare NCA particle and LYC-coated NCA particles prepared manually or mechanically are shown in Fig. 1c-e. An attempt to manually coat NCA particles was not successful; the surface coverage of NCA by LYC was poor (Fig. 1d). In contrast, the mechanical coating yielded a surface morphology with maximum LYC coverage of the NCA particle surface (Fig. 1e). The excellent surface coverage for the mechanically coated NCA particles is confirmed by cross-sectioned SEM images and the corresponding energy dispersive X-ray spectroscopy (EDXS) elemental maps displayed in Fig. 1f-h. The high-resolution XRD pattern of the LYC-coated NCA particles also confirms the intactness of the NCA crystal without the evolution of any impurity phases during the mechanical coating process and the presence of the trigonal Li_3YCl_6 phase despite the low crystallinity (Supplementary Fig. S1).

Electrodes with LYC-coated NCA were prepared with varying the LYC/LPSCl ratio: the NCA/LYC/LPSCl/C composition was 70:*x*:(30-*x*):3 by weight. Electrochemical performance results of NCA/Li-In half-cells cycled from 3.0 to 4.3 V (vs. Li/Li^+) at 30 °C for the NCA electrodes with the LYC fractions with respect to NCA of 0 (43 wt% LPSCl), 7, 10, 14, and 43 wt% (no LPSCl) are shown in Fig. 2 and summarized in Supplementary Table S1. Data of the electrodes with the full compositions (0, 3, 5, 7, 10, 12, 14, and 43 wt% LYC) are also provided in Supplementary Fig. S2. The first-cycle charge-discharge voltage profiles in Fig. 2a show that the capacity and overpotential vary largely with the LYC fraction. Notably, an electrode with 10 wt% LYC presented the highest discharge capacity of 202 mA h g^{-1}, which is much higher compared with the electrodes with only LPSCl (0 wt% LYC, 171 mA h g^{-1}) and that with only LYC (191 mA h g^{-1}). Consistently, the highest rate capability was recorded by the hybrid catholyte with 10 wt% LYC (Fig. 2b). These results are attributed to the synergistic effects of LYC and LPSCl: the former protects the NCA surface from LPSCl while the latter facilitates Li^+ conduction. Consistently, by coating with LYC, the initial Coulombic efficiencies (ICEs) were improved remarkably: e.g., 81.6% for 10 wt% LYC vs. 74.1% for 0 wt% LYC.

The cycling performances and capacity retention after 100 cycles for the LYC-coated NCA electrodes are compared in Fig. 2c and d, respectively. By increasing the LYC fraction from 0 to 7, 10, and 14 wt%, the capacity retention remarkably increased from 59% to 75.5%, 84.7%, and 86.6%, respectively. This result demonstrates the effect of the excellent (electro)chemical stability of LYC, and the trend follows the surface coverage of LYC on NCA. However, it is noted that the capacity retention for the electrode using only LYC (83.1%) was slightly lower compared to the electrodes with the hybrid catholytes using 10 or 14 wt % LYC. In a previous study, it was revealed that the unsatisfactory cycling performance of cathodes using LYC originated from the poor spatial distribution of particles, caused by the use of heavy LYC, which was susceptible to detrimental electrochemo-mechanical degradation. [31] Hence, the below-par cycling performance when only LYC was used in this study could thus be understood.

Specific energy densities for the NCA electrodes with hybrid catholytes at two different C-rates of 0.1C and 2C were calculated based on the weight of cathodes only, and the results are compared in Fig. 2e. The corresponding power densities are also plotted in Supplementary Fig. S3. The maximum values of the specific energy and power densities were observed for the electrodes with the 10 or 12 wt% LYC; specifically, the distinctly highest values were obtained for the electrodes with 10 wt% LYC, and the corresponding electrode was thus selected for further characterization.

The evolution of interfacial resistances upon cycling for the LYC-coated (10 wt%) NCA electrode was assessed by EIS measurements and compared with the results of the electrode without LYC. Nyquist plots for NCA/Li-In half-cells at 30 °C are presented in Fig. 3a-c. The figures show the archetypal feature of depressed semicircles followed by Warburg tails, which are attributed to the interfacial resistance and Li^+ diffusion in CAMs, respectively. [30,31] The data fitted using an equivalent circuit model shown in Supplementary Fig. S4a are also provided in Supplementary Fig. S4b, c and Supplementary Table S2. For both samples, the resistances of the separating SE layers corresponding to R1 + R2 were approximately 30 Ω and remained almost constant upon cycling. In contrast, a substantial difference in the amplitude of semicircle was observed between the samples. At the 2nd cycle, the large semicircle observed for the electrodes without LYC, reflecting an interfacial resistance of 61 Ω (R3), is in contrast to the much smaller semicircle observed for the electrodes with 10 wt% LYC, corresponding to 1.8 Ω. Moreover, the interfacial resistance for the electrode without LYC drastically increased to 169 and 501 Ω after 10 and 100 cycles,

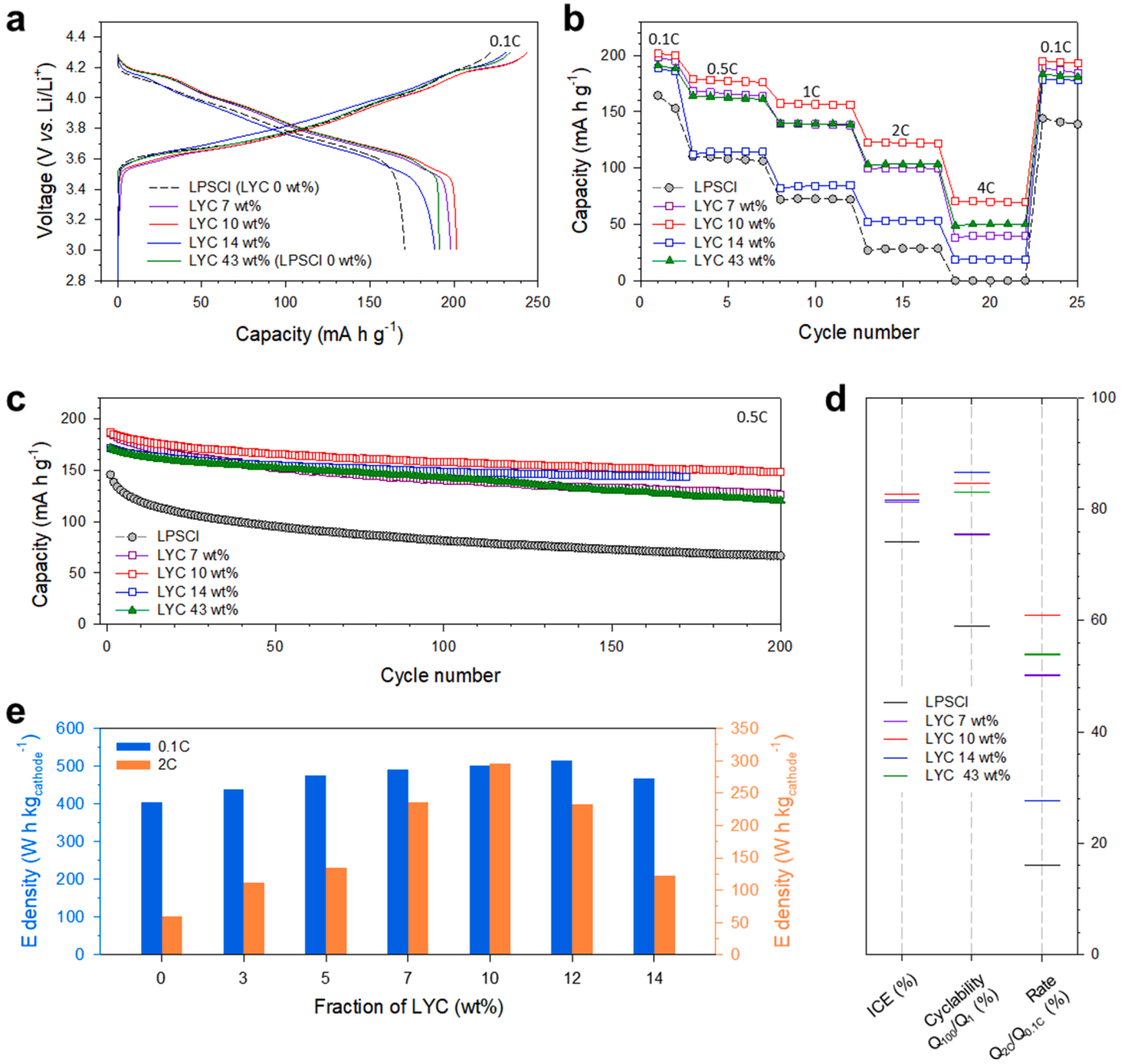

Fig. 2. Comparative electrochemical results of NCA electrodes without or with LYC coatings in all-solid-state half cells at 30 °C. a) First-cycle charge-discharge voltage profiles at 0.1C, and their corresponding b) rate capability and c) cycling performances at 0.5C. d) Comparative chart of cell performances of the electrodes. e) Energy density at 0.1C and 2C as a function of weight fraction of LYC with respect to NCA.

respectively. In contrast, the interfacial resistance at the 100th cycle for the electrodes with 10 wt% LYC was only 7.7 Ω.

To further assess the effects of interfacial side reactions in NCA cathodes without LYC or with 10 wt% LYC, an EIS experiment was performed using Li^+-non-blocking electron-blocking Li-In/LPSCl/cathode/LPSCl/Li-In symmetric cells, which allowed to extract the ionic conductivity of composite cathodes, σ_{ion}, as illustrated in Fig. 3d. [49] To rule out the effects of the side reactions caused by carbon, electrodes fabricated without carbon additives were employed. [49,61] The corresponding Nyquist plots at 30 °C for the electrodes before and after cycling are shown in Fig. 3e, f, and the resulting fitted σ_{ion} values are displayed in Fig. 3g. σ_{ion} is affected by the catholyte and NCA, and the Li^+ diffusion kinetics in NCA varies with the state of charges (SOCs). [62] For the cycled samples, discharge was carried out at the elevated temperature of 60 °C and low C-rate of 0.05C with the constant current-constant voltage (CCCV) mode (a limiting current of 0.001C). Thus, the SOCs for the two samples could be made identical, thereby excluding the effects of different Li^+ conductivities of NCA on the difference in σ_{ion}. [30,62] The pristine electrodes exhibited a smaller semicircle compared to the electrodes with 10 wt% LYC, which is not surprising considering the higher Li^+ conductivity of LPSCl (1.8 mS cm^{-1}) compared to that of LYC (0.4 mS cm^{-1}). However, after cycling (discharge), their amplitude became reversed: the amplitude of the semicircle for the electrode with 10 wt% LYC was smaller than that for the electrode without LYC. This result is summarized in the σ_{ion} plots shown in Fig. 3g, wherein the increasing σ_{ion} values upon cycling for the electrode with 10 wt% LYC are distinctly in contrast to the decreasing σ_{ion} values for the electrode without LYC. Consistently, the transient

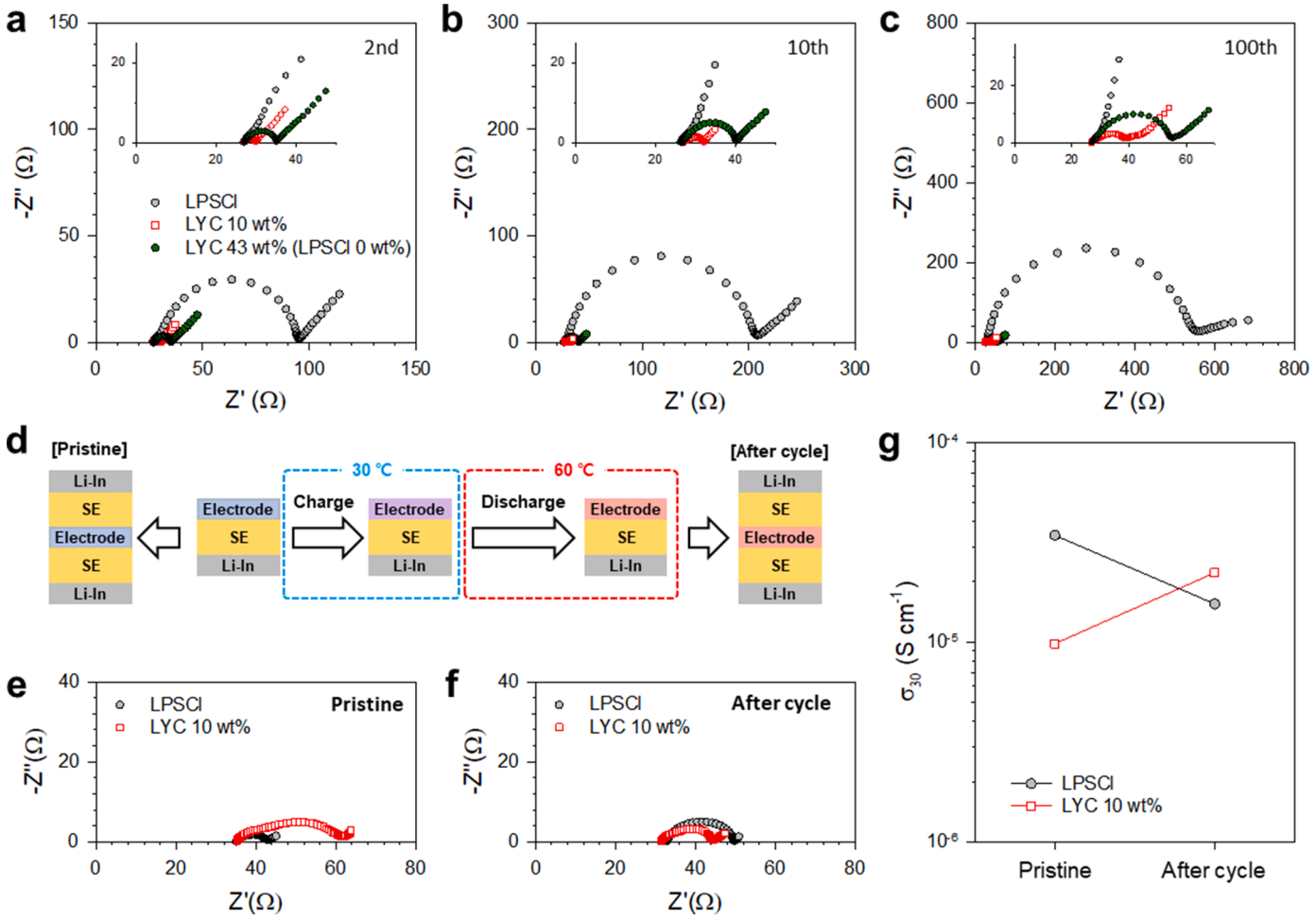

Fig. 3. Electrochemical impedance spectroscopy (EIS) results at 30 °C for NCA electrodes without or with LYC coatings. Nyquist plots for the electrodes of bare and LYC-coated NCA in NCA/Li-In all-solid-state cells at the a) 2nd, b) 10th, and c) 100th cycles. d) Schematic of the EIS measurements of the Li-In/LPSCl/electrode/LPSCl/Li-In symmetric cells. Corresponding Nyquist plots for the electrodes of bare and LYC-coated NCA e) before cycling and f) after discharge to 4 V (V *vs.* Li/Li^+) at 60 °C. g) Corresponding Li^+ conductivities at 30 °C.

discharge voltage profiles obtained by galvanostatic intermittent titration technique (GITT) and self-discharge test results exhibited a substantially lower polarization when using 10 wt% LYC compared to the electrode without LYC (Supplementary Figs. S5, S6).

The SOCs of the electrodes without LYC and with 10 wt% LYC were traced by in situ XRD measurements (Fig. 4). The (003) peaks reflecting the lattice parameter on the c-axis of the NCA structure serve as an indicator for SOCs. [30,31,63,64] First-cycle charge-discharge voltage profiles for the electrodes are shown in Fig. 4a, and the corresponding evolution of the (003) peaks for the electrodes with 10 wt% LYC and without LYC are displayed in Fig. 4b and c, respectively. Further, the corresponding changes in 2θ values, i.e., $2(\theta - \theta_{pristine})$, are plotted in Fig. 4d. The full-range in situ XRD data are shown in Supplementary Fig. S7. Several features are noteworthy: First, during the initial charge up to approximately 4 h, the electrode with 10 wt% LYC exhibited a distinctly larger shift in the position of the (003) peak compared to the electrode without LYC (highlighted by an enlarged view in the inset of Fig. 4d), indicating that substantial amounts of Li^+ were lost due to the side reaction for the electrode without LYC. Second, at the end of the charge, the shift in the position of the (003) peak was significantly larger for the electrode with 10 wt% LYC than that without LYC, reflecting a higher SOC. This result is explained by the favorable NCA-LYC interfaces exhibiting low interfacial resistances, which is also in agreement with the EIS and GITT results. Third, at the end of discharge, the (003) peak position returned more closely to the original position for the electrode with 10 wt% LYC, compared with the electrode without LYC, indicating the higher depth of discharge.

To probe the NCA-SE interfacial evolution varying with the LYC coating, ex situ TEM and XPS measurements were conducted for the electrodes without LYC and with 10 wt% LYC before cycling and after 100 cycles, and the results are compared in Fig. 5. The fitted XPS results are summarized in Supplementary Table S3. Carbon additives were not included in the electrodes to exclude the effects of SE decomposition due to carbon. [49,61] TEM images of the electrodes without LYC and with 10 wt% LYC and the corresponding fast Fourier transformed (FFT) patterns are shown in Fig. 5a and b, respectively. For the electrode without LYC, the bulk region (i) exhibited the retention of the original layered structure with $R\bar{3}m$ symmetry. However, the surface region (ii) that is in contact with the LPSCl layer exhibited a NiO-like rocksalt structure with $Fm\bar{3}m$ symmetry. This rocksalt phase has been documented as the culprit for the degradation of Li^+ kinetics and could be formed with the oxidation of LPSCl, driven by the high reactivity of Ni^{4+} in a charged NCA. [30,31] In contrast, for the electrode with 10 wt% LYC, the crystal structure for both bulk and surface regions exhibited the same layered structure with $R\bar{3}m$ symmetry, confirming the excellent stability of LYC. Ex situ XPS results for the electrode without LYC in Fig. 5c exhibited the formation of oxidized species including PO_4^{3-}, SO_4^{2-}, bridging sulfur (P-$[S]_n$-P), and P_2S_5 after cycling, reflecting the severe oxidation of LPSCl. [26,30,31,33,65] Specifically, the oxygen released from NCA accounts for the rocksalt phase transformation along

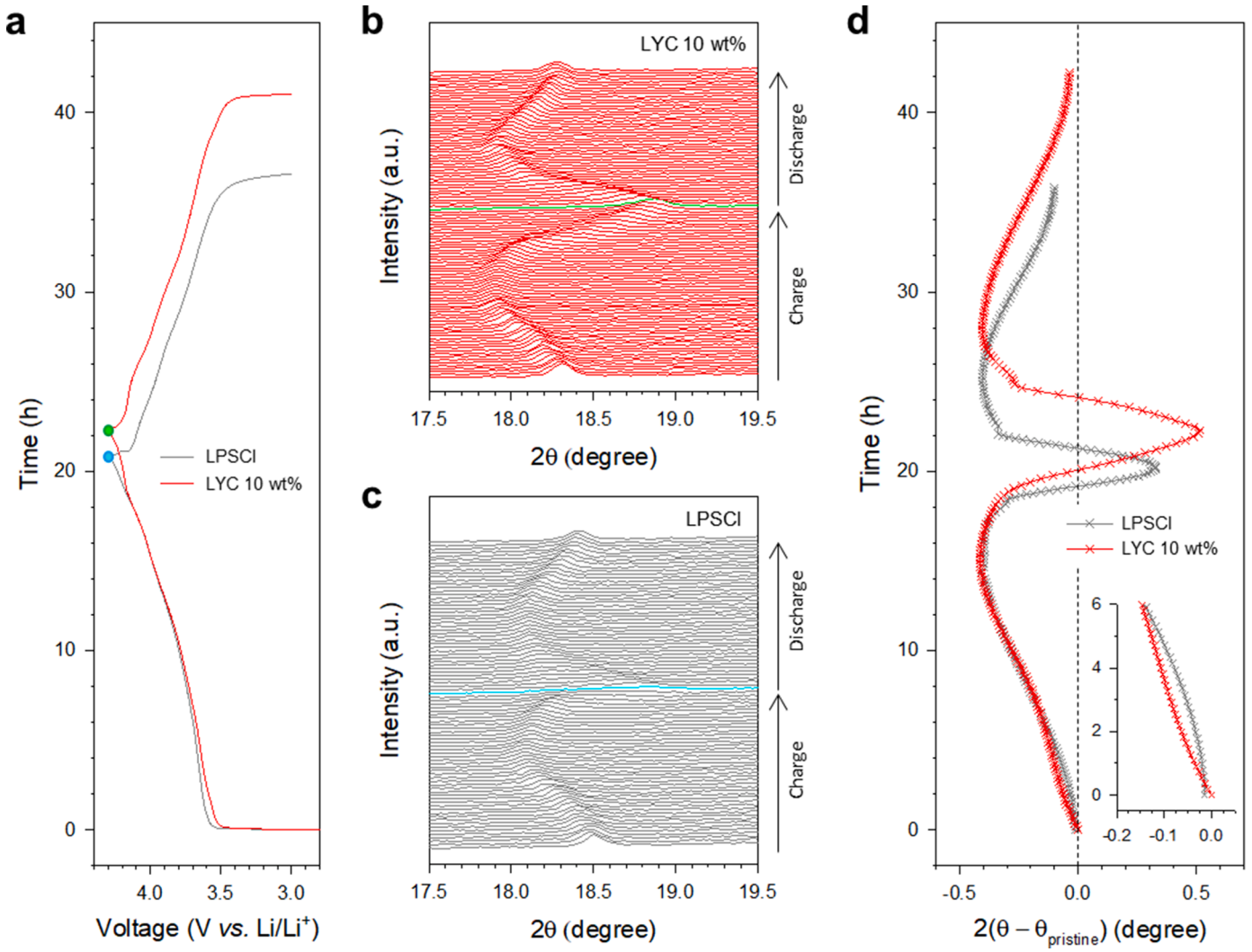

Fig. 4. In situ XRD results of bare and LYC-coated (10 wt%) NCA electrodes in all-solid-state half-cells at room temperature. a) First-cycle charge-discharge voltage profiles and the corresponding in situ XRD patterns showing the evolution of the (003) peaks for the NCA electrodes b) with 10 wt% LYC coating and c) without LYC coating. d) Corresponding changes in the (003) peak position, $2(\theta - \theta_{pristine})$.

with the uptake of oxygen by Li_6PS_5Cl. Ex situ XPS spectra for the electrode with 10 wt% LYC are shown in Fig. 5d. The P 2p spectra for the electrode with 10 wt% LYC also showed the Li_6PS_5Cl-derived oxidized species, which should evolve in the interfacial region which LYC did not protect. However, the fractions of the oxidized species in the electrode with LYC were much lower compared with the electrode without LYC (Supplementary Table S3). Interestingly, the Y 3d spectrum after cycling exhibited an unexpected evolution of Y_2O_3. In previous studies, LYC did not suffer from any oxidation when employed as a single catholyte for $LiMO_2$. [31,32] Moreover, the surface region of the NCA particle that was in contact with LYC retained its original layered crystal structure (Fig. 5b). From these results, the oxidation of LYC after cycling is seen to be coupled with the oxidation of Li_6PS_5Cl, implying that the suppression of oxidation of halide SEs in the hybrid catholyte could be important for further improvements.

Electrochemical performance of an NCA electrode coated with another halide SE Li_3InCl_6 (10 wt%) was also assessed. Despite the higher Li^+ conductivity of Li_3InCl_6 (1.0 mS cm^{-1}) than that of LYC (0.4 mS cm^{-1}), the Li_3InCl_6-coated electrode exhibited the lower capacities and poorer cycling performance compared with the LYC-coated electrode (Supplementary Fig. S8). This result is contrasted by stable cycling performances in previous results for which Li_3InCl_6 was employed as a single catholyte, [39] and it indicates that incompatibility between halide and sulfide SEs strongly affect the electrochemical performance. Consistently, Koc et al., reported that the electrochemical degradation at the triple-phase Li[Ni,Co,Mn]O_2-LPSCl-Li_3InCl_6 contact point within a composite is caused by the chemical incompatibility between Li_3InCl_6 and LPSCl. [66]

To explain the effects of various design factors on NCA cathodes with hybrid catholytes, digital twin-driven 3D structural modeling was conducted. Four NCA electrode structures with the different fractions of LYC coatings (0, 7, 10, and 14 wt%) were generated while the spatial arrangement of NCA particles was maintained (Fig. 6a). As illustrated in Fig. 6b, three structural parameters that are inaccessible by experiments were carefully chosen and varied for the simulations: i) Li^+ conductivity and ii) thickness of the impurity layers and (iii) thickness of the LYC layers. To begin with, the characteristic Li^+ conductivity and thickness of the impurity layers were assessed. Specifically, the voltage profiles for the bare electrode structures were simulated by varying the thickness (0.25, 0.50, and 0.75 μm) and Li^+ conductivity (10^{-3}, 10^{-4}, and 10^{-5} times that of LPSCl) of the impurity layers at the interface of the bare CAM and LPSCl (Supplementary Fig. S9a-c). These thickness and Li^+ conductivity ranges were set reflecting the TEM image (Fig. 5a) and a literature value, [67] respectively. Among nine simulated voltage profiles of each combination, the structure with the 0.25 μm thick and 10^{-5} times Li^+ conductive (compared to LPSCl) impurity layer was found to

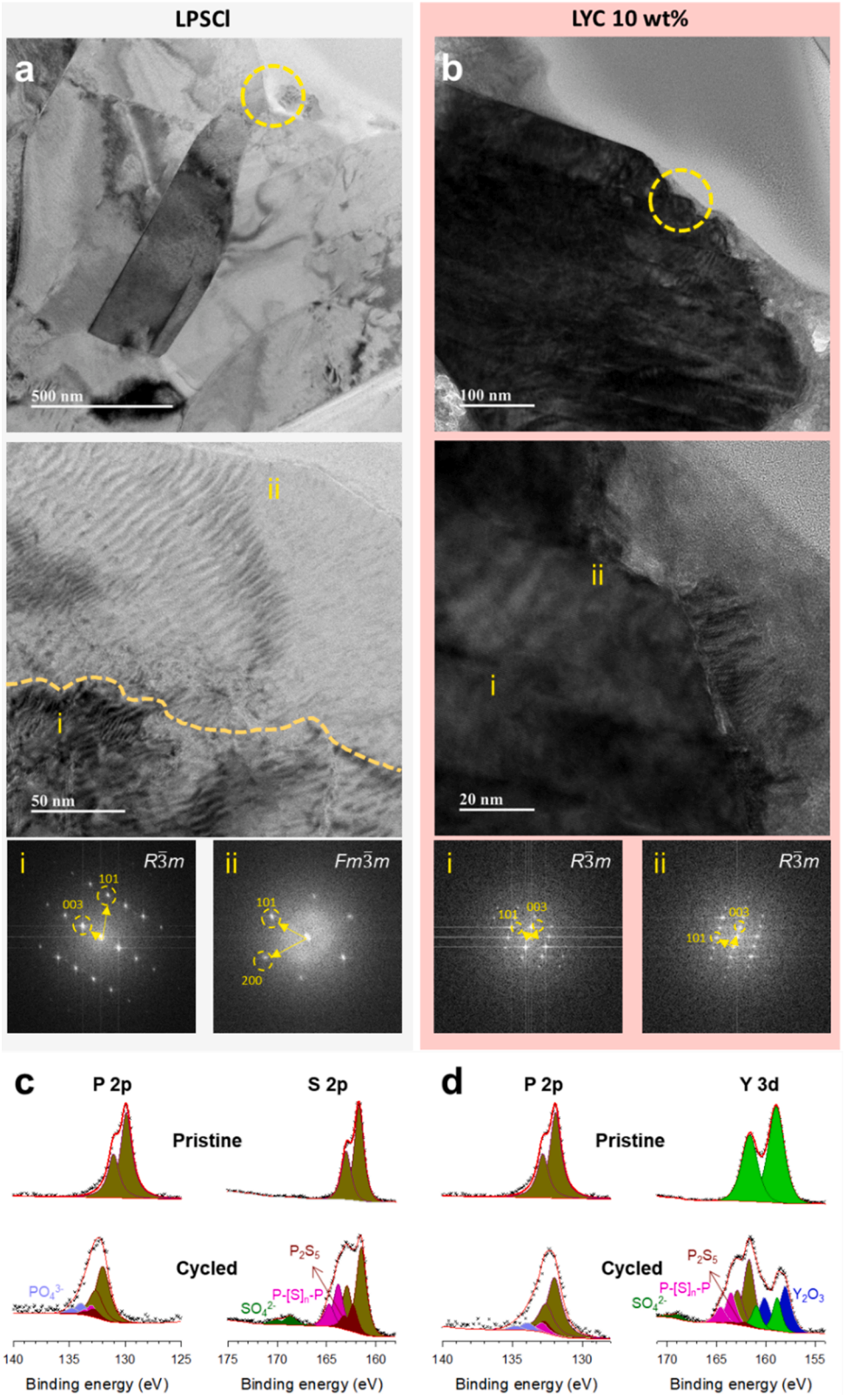

Fig. 5. Ex situ TEM and XPS results of bare and LYC-coated (10 wt%) NCA electrodes in all-solid-state cells cycled after 100 cycles at 30 °C. Low- and high-magnification ex situ TEM images for the surface regions of a) bare and b) LYC-coated NCA particles, and their corresponding FFT images. Note that bare and LYC-coated NCA particles are in contact with LPSCl and LYC, respectively. Ex situ XPS spectra for c) bare and d) LYC-coated NCA electrodes before cycling and after cycles.

best match with the corresponding experimental voltage profile shown in Supplementary Fig. S9d, which were considered as fixed conditions in further simulations. After that, the thickness of LYC coating (0.5-1.5 μm and 0.5-3.0 μm) could be optimized to obtain reliable simulated voltage profiles that were comparable to the experimental results (Figs. 6c, S9e). Our systematic approaches, thus, could build the virtual 3D electrode structures having reliable physical properties.

In the established 3D electrode structure, experimentally veiled parameters such as the contact area between NCA and other electrode components could be quantified, and the results are summarized in Tables S4, S5. Moreover, digital twin modeling could visualize the electronic current density of the LYC-coated NCA electrodes (Fig. 6d).

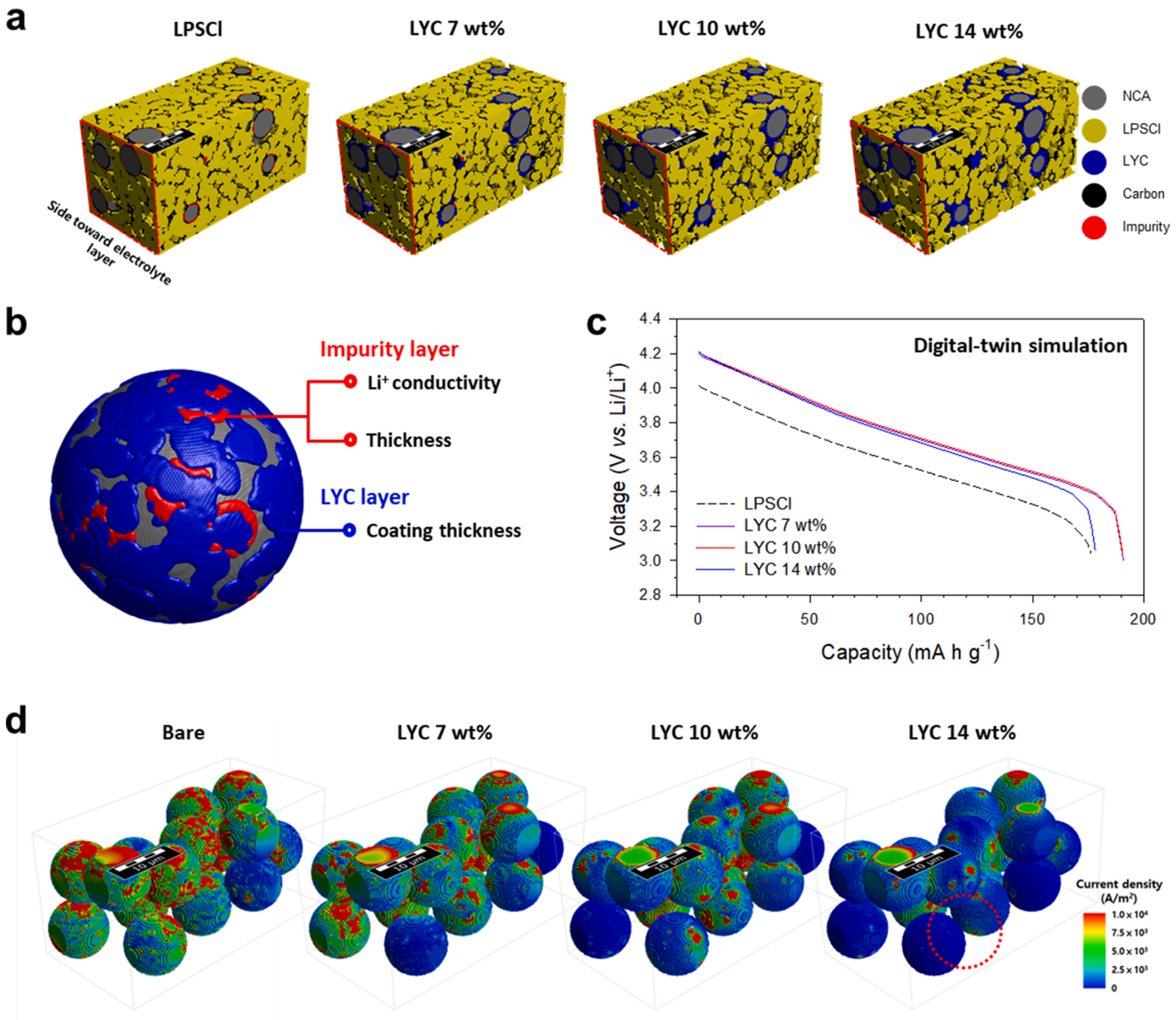

Fig. 6. 3D digital twin modeling results of LYC-coated NCA electrodes and the corresponding guided electrochemical results. a) 3D digital twin of the bare and LYC-coated NCA all-solid-state electrodes. b) Scheme illustrating parameters controlled in the LYC-coated NCA. c) Digital twin-simulated discharge voltage profiles of the bare and LYC-coated NCA electrodes with the LYC coating thicknesses of 0.5-1.5 μm and d) the corresponding electronic current density in the NCA structures.

Notably, increasing the amount of LYC coatings to 14 wt%, some NCA particles almost lost the electronic connection (indicated by a red circle), which was due to the significantly reduced contact area percentage between NCA and carbon additives; e.g., the surface coverage of NCA by carbon for 14 wt% was 11.46% vs. 15.69% for 10 wt% (Supplementary Table S4).

To overcome the digital twin-identified insufficient activation of the NCA particles, a coating protocol was devised using a mixed-conducting phase of LYC-C composites. Specifically, the mixed-conductor coating process proceeded as illustrated in Fig. 7a. On the 10 wt% LYC-coated NCA particles, 4 wt% LYC and 1.4 wt% (with respect to NCA) carbon additives were dry-coated. Subsequently, the LYC-C-coated NCA particles were manually mixed with LPSCl and additional carbon additives (2.8 wt%), resulting in the same electrode composition as the 14 wt% LYC-coated NCA electrode (the NCA/LYC/LPSCl/carbon weight ratio was 70.0:9.8:20.2:3.0). In Fig. 7b, c, the discharge voltage profile at 0.5C and rate capability for the LYC-C-coated NCA electrode are compared with those for the conventional LYC-coated NCA electrodes. The LYC-C-coated NCA electrode substantially outperformed the LYC-coated NCA electrode with the same electrode composition (14 wt% LYC); e.g., 134 vs. 53 mA h g^{-1} at 2C. Moreover, the rate capability of the LYC-C-coated NCA electrode with 14 wt% LYC was also higher than that of the LYC-coated NCA electrode with the optimal LYC fraction of 10 wt% (122 mA h g^{-1} at 2C). This experimental result confirms the sound diagnosis guided by the established 3D digital twin modeling and thus highlights its validity.

Despite the successful optimization of the LYC-C-coated electrodes, a remaining concern is a decomposition of LPSCl on the surface of carbon additives. [68] Thus, a control (LYC-C-coated) electrode sample was prepared so that carbon was excluded in the LPSCl region (Supplementary Fig. S10a). The control electrode showed slightly improved capacity retention but at the expense of significantly decreased capacity at 0.5C (Supplementary Fig. S10b, S10c), indicating that electrical wiring through the LPSCl region in the hybrid catholyte is necessary for optimal rate performance. Thus, an engineering to suppress side reactions at the surface of carbon additives is needed for further

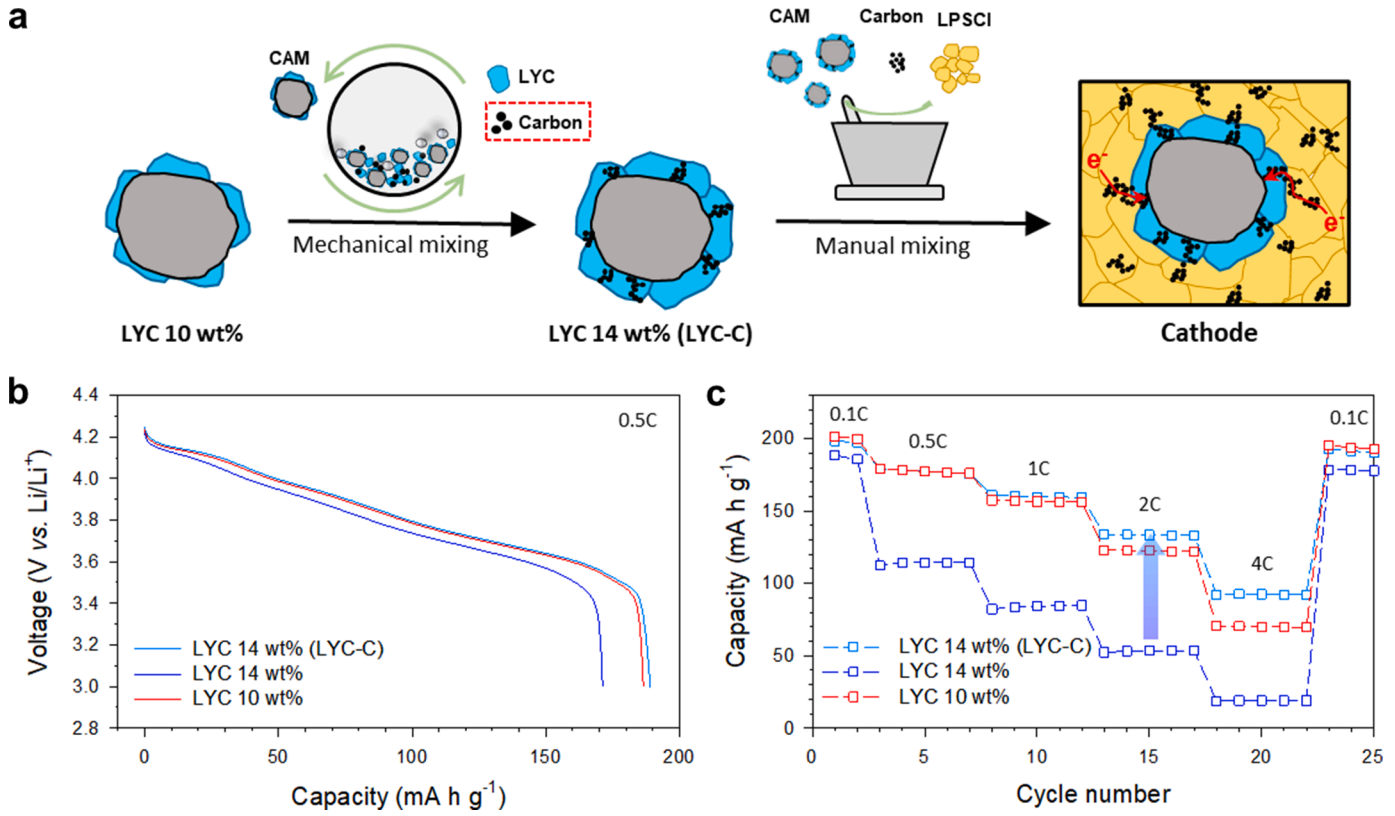

Fig. 7. Digital twin-guided LYC-C-coated NCA electrodes. a) Schematic of the digital twin-guided design of LYC-C-coated NCA electrodes for which carbon additives and LYC are added to facilitate electronic conduction pathways. b) First-cycle charge-discharge voltage profiles at 0.5C and 30 °C for LYC-C (or LYC) coated electrodes and c) the corresponding rate capabilities.

improvements, which is our future mission. [69,70]

3. Conclusions

In summary, a rational design of a new sulfide-halide catholyte that complements the disadvantages of sulfide and halide was suggested for Ni-rich layered oxide cathodes used in ASLBs. A 10 wt% LYC coating on NCA resulted in optimal electrochemical performance in terms of discharge capacity (202 mA h g^{-1} at 0.1C), rate capability, and cycling performance. The EIS analyses using NCA/Li-In half-cells and Li-In/SE/electrode/SE/Li-In symmetric cells confirmed the superior interfacial stability for the LYC-coated electrode over the electrode without LYC. Consistently, in situ XRD results disclosed a wider range of the utilization of NCA when using an LYC-coated electrode, compared to the electrode without LYC. Additionally, the effective protection of NCA by LYC from the side reactions caused by LPSCl could be validated by the ex-situ TEM and XPS measurements. However, the unexpected evolution of Y_2O_3 from LYC was observed after cycling, which might be coupled with the side reaction of sulfide SE LPSCl. This result thus emphasizes a research direction about sulfide-halide compatibility. Moreover, digital twin modeling, which made it possible to vary several parameters that are hard to investigate by experiments, could simulate composite NCA cathodes with hybrid catholytes successfully. Importantly, the digital twin modeling results revealed insufficient electrical contacts when very large quantities of LYC coatings were employed (14 wt%), leading to a further enhancement in electrochemical performance by the development of the mixed conductor coating comprised of LYC-C. The hybrid inorganic SE design suggested in this study is of significance in practical ASLB technologies as well as gives rise to many intriguing scientific issues such as SE compatibility. In addition, the digital twin-guided design of composite electrodes herein offers an important insight into the design of ASLB composite electrodes.

4. Experimental methods

4.1. Preparation of materials

For the preparation of Li_3YCl_6 powders, a stoichiometric mixture of LiCl (99.99%, Sigma Aldrich) and YCl_3 (99.99%, Sigma Aldrich) was ball-milled at 600 rpm for 10 h in a ZrO_2 vial with ZrO_2 balls. LYC-coated NCA powders were prepared via ball-milling a mixture of NCA and LYC with a total amount of 2.2 g at 200 rpm for 1 h in a ZrO_2 vial with ZrO_2 balls. NCA an LPSCl powders were provided by EcoPro BM Co. Ltd. and CIS Co. Ltd., respectively.

4.2. Materials characterization

An XRD measurement of LYC-coated NCA powders was performed with Cu K_α radiation (1.5418 Å) using a high-resolution X-ray diffractometer (Smartlab, Rigaku). The XRD data were collected between 10 and 110° with a step size of 0.02. In situ XRD measurements for NCA/Li-In half cells were performed using a custom-made all-solid-state cell (Supplementary Fig. S11). The in situ XRD cells were charged and discharged between 3.0 and 4.3 V (vs Li/Li^+) by applying a constant current of 0.05C (9 mA g^{-1}) at room temperature and under an applied pressure of ~1 MPa. The in situ XRD data were continuously recorded in the range of 15–50° at a step width of 0.02° with Cu K_α radiation (1.5406 Å) using Rigaku MiniFlex 600 diffractometer. SEM measurements were performed using Verios G4UC (FEI). For the ex-situ TEM measurements, electrodes that were cycled 100 times at the discharged state (3 V vs Li/Li^+) were collected and cut into a 70-nm-thick foil using a focused ion beam (FIB, SCIOS, FEI), and loaded onto a Mo grid. The voltage of the ion beam was 30 and 5 kV for etching and cleaning, respectively. The ex-situ XPS measurements were carried out with a monochromatic Al K_α source (1486.6 eV) at 12 kV and 6 mA using K-Alpha+ (Thermo Fisher

Scientific). The samples were mounted on a sample holder in an Ar-filled glove box and transferred into the XPS equipment without any exposure to air.

4.3. Electrochemical characterization

For the preparation of NCA electrodes in all-solid-state cells, a mixture of NCA (or LYC-coated NCA), SE (LPSCl or LYC), and conductive carbon additives (super C65) were dry-mixed in a weight ratio of 70:30:3 using mortar and pestle. The Li-In counter electrodes (or reference electrodes), which were partially lithiated indium (nominal composition of $Li_{0.5}In$), were prepared by mixing Li (FMC Lithium Corp.) and In (Aldrich, 99%) powders. All-solid-state cells with a diameter of 13 mm, comprised of Ti rods as the current collectors and poly-aryletheretherketone (PEEK) mold, were assembled by the following procedure. After SE layers were formed by pelletizing 150 mg of LPSCl powders (≈ 610 μm), the counter electrode ($Li_{0.5}In$) was placed on one side of the SE layer. After the as-prepared cathode mixture was spread on the other side of the SE layer, the assemblies were pressed at 370 MPa. The mass loading of the NCA electrodes was 11.3 mg cm^{-2}. The EIS measurements were performed for the cells discharged to 3.8 V (vs. Li/Li^+) at 0.1C using a Bio-Logic (VMP3) from 1.5 MHz to 5 mHz with an amplitude of 10 mV. The external pressure of the all-solid-state cells during the operation was ≈70 MPa.

4.4. Digital twin modeling of 3D all-solid-state electrode structures

The 3D structures of all-solid-state electrodes used in this study were generated by GeoDict 2022 (Math2Market, Germany). The 3D electrode structures were designed with a loading level of 11.3 mg cm^{-2} and a thickness of 50 μm. The porosity of the bare and LYC-coated electrodes was set to 18.63 and 23.75%, respectively. Additionally, NCA particles were formed as spherical particles through the “Create Grains” function. The LYC SEs were formed on the surface of the NCA particles through the “Create Grains” function in the GrainGeo module. LPSCl SE particles were also produced as spherical particles. The impurity layer described the side reaction products formed at the interface between NCA and LPSCl. Lastly, carbon additives were formed using the "Add binder" function in the GrainGeo module. The domain size of all electrode structures was set to 25 × 25 × 50 $μm^3$, and the voxel length was set to 0.25 μm. To quantify the contact area between electrode components, the numerical value was quantified using the MatDict module.

4.5. Electrochemical simulation for 3D all-solid-state electrode model

The 3D battery model using 3D all-solid electrode structures was simulated after forming 3D structures of batteries comprising lithium metal, LPSCl SE layer, and 3D all-solids-state electrode structures. The parameters are summarized in Supplementary Table S5. A detailed description of each equation can be found in previous studies. [58,60] To confirm the effect of the LYC coating on NCA, Li^+ concentration and overpotential on NCA particles were simulated through electrochemical modeling during the 0.5C-rate discharge at 30 °C. Subsequently, the results for the LYC coating effect on the NCA surface were compared at 3.0 V (*vs.* Li/Li^+).

CRediT authorship contribution statement

Jong Seok Kim: Conceptualization, Methodology, Investigation, Writing – original draft. **Seungwon Jung:** Methodology, Investigation, Writing – original draft. **Hiram Kwak:** Investigation. **Yoonjae Han:** Data curation. **Suhwan Kim:** Resources. **Jongwoo Lim:** Writing – review & editing. **Yong Min Lee:** Supervision, Writing – review & editing. **Yoon Seok Jung:** Conceptualization, Supervision, Writing – review & editing.

Declaration of Competing Interest

The authors declare that they have no known competing financial interests or personal relationships that could have appeared to influence the work reported in this paper.

Acknowledgements

Jong Seok Kim and Seungwon Jung contributed equally to this work. This work was supported by the National Research Foundation of Korea (NRF) funded by the Ministry of Science, ICT & Future Planning (NRF-2022M3J1A1085397), by the Human Resources Development Program (No. 20214000000320) of the Korea Institute of Energy Technology Evaluation and Planning (KETEP), funded by the Ministry of Trade, Industry and Energy of the Korean government, by the Samsung Science and Technology Foundation under project no. SRFC-MA2002-04, and by the Yonsei University Research Fund of 2022 (2022-22-0284).

Supplementary materials

Supplementary material associated with this article can be found, in the online version, at doi:10.1016/j.ensm.2022.11.038.

References

[1] J. Janek, W.G. Zeier, A solid future for battery development, Nat. Energy 1 (2016) 16141, https://doi.org/10.1038/nenergy.2016.141.
[2] A. Manthiram, X. Yu, S. Wang, Lithium battery chemistries enabled by solid-state electrolytes, Nat. Rev. Mater. 2 (2017) 16103, https://doi.org/10.1038/natrevmats.2016.103.
[3] R. Chen, Q. Li, X. Yu, L. Chen, H. Li, Approaching practically accessible solid-state batteries: stability issues related to solid electrolytes and interfaces, Chem. Rev. 120 (2020) 6820–6877, https://doi.org/10.1021/acs.chemrev.9b00268.
[4] Y. Kato, S. Hori, T. Saito, K. Suzuki, M. Hirayama, A. Mitsui, M. Yonemura, H. Iba, R. Kanno, High-power all-solid-state batteries using sulfide superionic conductors, Nat. Energy 1 (2016) 16030, https://doi.org/10.1038/nenergy.2016.30.
[5] K.H. Park, Q. Bai, D.H. Kim, D.Y. Oh, Y. Zhu, Y. Mo, Y.S. Jung, Design strategies, practical considerations, and new solution processes of sulfide solid electrolytes for all-solid-state batteries, Adv. Energy Mater. 8 (2018), 1800035, https://doi.org/10.1002/aenm.201800035.
[6] J. Schnell, T. Günther, T. Knoche, C. Vieider, L. Köhler, A. Just, M. Keller, S. Passerini, G. Reinhart, All-solid-state lithium-ion and lithium metal batteries – paving the way to large-scale production, J. Power Sources 382 (2018) 160–175, https://doi.org/10.1016/j.jpowsour.2018.02.062.
[7] Z. Zhang, Y. Shao, B. Lotsch, Y.-S. Hu, H. Li, J. Janek, L.F. Nazar, C.-W. Nan, J. Maier, M. Armand;, et al., New horizons for inorganic solid state ion conductors, Energy Environ. Sci. 11 (2018) 1945–1976, https://doi.org/10.1039/c8ee01053f.
[8] Q. Zhang, D. Cao, Y. Ma, A. Natan, P. Aurora, H. Zhu, Sulfide-based solid-state electrolytes: synthesis, stability, and potential for all-solid-state batteries, Adv. Mater. 31 (2019), 1901131, https://doi.org/10.1002/adma.201901131.
[9] Y.-G. Lee, S. Fujiki, C. Jung, N. Suzuki, N. Yashiro, R. Omoda, D.-S. Ko, T. Shiratsuchi, T. Sugimoto, S. Ryu;, et al., High-energy long-cycling all-solid-state lithium metal batteries enabled by silver–carbon composite anodes, Nat. Energy 5 (2020) 299–308, https://doi.org/10.1038/s41560-020-0575-z.
[10] L. Duchêne, D.H. Kim, Y.B. Song, S. Jun, R. Moury, A. Remhof, H. Hagemann, Y. S. Jung, C. Battaglia, Crystallization of closo-borate electrolytes from solution enabling infiltration into slurry-casted porous electrodes for all-solid-state batteries, Energy Storage Mater. 26 (2020) 543–549, https://doi.org/10.1016/j.ensm.2019.11.027.
[11] M.J. Wang, E. Kazyak, N.P. Dasgupta, J. Sakamoto, Transitioning solid-state batteries from lab to market: linking electro-chemo-mechanics with practical considerations, Joule 5 (2021) 1371–1390, https://doi.org/10.1016/j.joule.2021.04.001.
[12] Z. Yu, S.L. Shang, K. Ahn, D.T. Marty, R. Feng, M.H. Engelhard, Z.K. Liu, D. Lu, Enhancing moisture stability of sulfide solid-state electrolytes by reversible amphipathic molecular coating, ACS Appl. Mater. Interfaces 14 (2022) 32035–32042, https://doi.org/10.1021/acsami.2c07388.
[13] K. Kerman, A. Luntz, V. Viswanathan, Y.-M. Chiang, Z. Chen, Review—practical challenges hindering the development of solid state Li ion batteries, J. Electrochem. Soc. 164 (2017) A1731–A1744, https://doi.org/10.1149/2.1571707jes.
[14] X. Han, Y. Gong, K.K. Fu, X. He, G.T. Hitz, J. Dai, A. Pearse, B. Liu, H. Wang, G. Rubloff;, et al., Negating interfacial impedance in garnet-based solid-state Li metal batteries, Nat. Mater. 16 (2017) 572–579, https://doi.org/10.1038/nmat4821.
[15] K.H. Park, D.Y. Oh, Y.E. Choi, Y.J. Nam, L. Han, J.Y. Kim, H. Xin, F. Lin, S.M. Oh, Y. S. Jung, Solution-processable glass LiI-Li_4SnS_4 superionic conductors for all-solid-

state Li-Ion batteries, Adv. Mater. 28 (2016) 1874–1883, https://doi.org/10.1002/adma.201505008.
[16] H.-J. Deiseroth, S.-T. Kong, H. Eckert, J. Vannahme, C. Reiner, T. Zaiß, M. Schlosser, Li_6PS_5X: a class of crystalline li-rich solids with an unusually high Li^+ mobility, Angew. Chem. Int. Ed. 120 (2008) 767–770, https://doi.org/10.1002/ange.200703900.
[17] N.J.J. de Klerk, I. Rosłoń, M. Wagemaker, Diffusion mechanism of Li argyrodite solid electrolytes for Li-Ion batteries and prediction of optimized halogen doping: the effect of Li vacancies, halogens, and halogen disorder, Chem. Mater. 28 (2016) 7955–7963, https://doi.org/10.1021/acs.chemmater.6b03630.
[18] S. Chen, D. Xie, G. Liu, J.P. Mwizerwa, Q. Zhang, Y. Zhao, X. Xu, X. Yao, Sulfide solid electrolytes for all-solid-state lithium batteries: structure, conductivity, stability and application, Energy Storage Mater. 14 (2018) 58–74, https://doi.org/10.1016/j.ensm.2018.02.020.
[19] L. Zhou, N. Minafra, W.G. Zeier, L.F. Nazar, Innovative approaches to Li-argyrodite solid electrolytes for all-solid-state lithium batteries, Acc. Chem. Res. 54 (2021) 2717–2728, https://doi.org/10.1021/acs.accounts.0c00874.
[20] B.R. Shin, Y.J. Nam, D.Y. Oh, D.H. Kim, J.W. Kim, Y.S. Jung, Comparative study of TiS_2/Li-In all-solid-state lithium batteries using glass-ceramic Li_3PS_4 and $Li_{10}GeP_2S_{12}$ solid electrolytes, Electrochim. Acta 146 (2014) 395–402, https://doi.org/10.1016/j.electacta.2014.08.139.
[21] Y. Zhu, X. He, Y. Mo, Origin of outstanding stability in the lithium solid electrolyte materials: insights from thermodynamic analyses based on first-principles calculations, ACS Appl. Mater. Interfaces 7 (2015) 23685–23693, https://doi.org/10.1021/acsami.5b07517.
[22] A. Sakuda, A. Hayashi, M. Tatsumisago, Interfacial Observation between $LiCoO_2$ Electrode and Li_2S−P_2S_5 solid electrolytes of all-solid-state lithium secondary batteries using transmission electron microscopy, Chem. Mater. 22 (2009) 949–956, https://doi.org/10.1021/cm901819c.
[23] A. Banerjee, X. Wang, C. Fang, E.A. Wu, Y.S. Meng, Interfaces and interphases in all-solid-state batteries with inorganic solid electrolytes, Chem. Rev. 120 (2020) 6878–6933, https://doi.org/10.1021/acs.chemrev.0c00101.
[24] J. Haruyama, K. Sodeyama, L. Han, K. Takada, Y. Tateyama, Space–charge layer effect at interface between oxide cathode and sulfide electrolyte in all-solid-state lithium-ion battery, Chem. Mater. 26 (2014) 4248–4255, https://doi.org/10.1021/cm5016959.
[25] Y. Zhu, X. He, Y. Mo, First principles study on electrochemical and chemical stability of solid electrolyte–electrode interfaces in all-solid-state Li-ion batteries, J. Mater. Chem. A 4 (2016) 3253–3266, https://doi.org/10.1039/c5ta08574h.
[26] J. Auvergniot, A. Cassel, J.-B. Ledeuil, V. Viallet, V. Seznec, R. Dedryvère, Interface stability of argyrodite Li_6PS_5Cl toward $LiCoO_2$, $LiNi_{1/3}Co_{1/3}Mn_{1/3}O_2$, and $LiMn_2O_4$ in bulk all-solid-state batteries, Chem. Mater. 29 (2017) 3883–3890, https://doi.org/10.1021/acs.chemmater.6b04990.
[27] R. Koerver, I. Aygün, T. Leichtweiß, C. Dietrich, W. Zhang, J.O. Binder, P. Hartmann, W.G. Zeier, J. Janek, Capacity fade in solid-state batteries: interphase formation and chemomechanical processes in nickel-rich layered oxide cathodes and lithium thiophosphate solid electrolytes, Chem. Mater. 29 (2017) 5574–5582, https://doi.org/10.1021/acs.chemmater.7b00931.
[28] F. Walther, R. Koerver, T. Fuchs, S. Ohno, J. Sann, M. Rohnke, W.G. Zeier, J. Janek, Visualization of the interfacial decomposition of composite cathodes in argyrodite-based all-solid-state batteries using time-of-flight secondary-ion mass spectrometry, Chem. Mater. 31 (2019) 3745–3755, https://doi.org/10.1021/acs.chemmater.9b00770.
[29] S.-K. Jung, H. Gwon, S.-S. Lee, H. Kim, J.C. Lee, J.G. Chung, S.Y. Park, Y. Aihara, D. Im, Understanding the effects of chemical reactions at the cathode–electrolyte interface in sulfide based all-solid-state batteries, J. Mater. Chem. A 7 (2019) 22967–22976, https://doi.org/10.1039/c9ta08517c.
[30] S.H. Jung, U.H. Kim, J.H. Kim, S. Jun, C.S. Yoon, Y.S. Jung, Y.K. Sun, Ni-rich layered cathode materials with electrochemo-mechanically compliant microstructures for all-solid-state Li batteries, Adv. Energy Mater. 10 (2019), 1903360, https://doi.org/10.1002/aenm.201903360.
[31] Y. Han, S.H. Jung, H. Kwak, S. Jun, H.H. Kwak, J.H. Lee, S.T. Hong, Y.S. Jung, Single- or poly-crystalline ni-rich layered cathode, sulfide or halide solid electrolyte: which will be the winners for all-solid-state batteries? Adv. Energy Mater. 11 (2021), 2100126 https://doi.org/10.1002/aenm.202100126.
[32] T. Asano, A. Sakai, S. Ouchi, M. Sakaida, A. Miyazaki, S. Hasegawa, Solid halide electrolytes with high lithium-ion conductivity for application in 4 V class bulk-type all-solid-state batteries, Adv. Mater. 30 (2018), 1803075, https://doi.org/10.1002/adma.201803075.
[33] S.H. Jung, K. Oh, Y.J. Nam, D.Y. Oh, P. Brüner, K. Kang, Y.S. Jung, Li_3BO_3–Li_2CO_3: rationally designed buffering phase for sulfide all-solid-state Li-Ion batteries, Chem. Mater. 30 (2018) 8190–8200, https://doi.org/10.1021/acs.chemmater.8b03321.
[34] N. Ohta, K. Takada, L. Zhang, R. Ma, M. Osada, T. Sasaki, Enhancement of the high-rate capability of solid-state lithium batteries by nanoscale interfacial modification, Adv. Mater. 18 (2006) 2226–2229, https://doi.org/10.1002/adma.200502604.
[35] J.H. Woo, J.J. Travis, S.M. George, S.-H. Lee, Utilization of Al_2O_3 atomic layer deposition for li ion pathways in solid state Li batteries, J. Electrochem. Soc. 162 (2014) 344, https://doi.org/10.1149/2.0441503jes.
[36] Y. Ito, Y. Sakurai, S. Yubuchi, A. Sakuda, A. Hayashi, M. Tatsumisago, Application of $LiCoO_2$ particles coated with lithium ortho-oxosalt thin films to sulfide-type all-solid-state lithium batteries, J. Electrochem. Soc. 162 (2015) 1610, https://doi.org/10.1149/2.0771508jes.
[37] G. Oh, M. Hirayama, O. Kwon, K. Suzuki, R. Kanno, Bulk-type all solid-state batteries with 5 V Class $LiNi_{0.5}Mn_{1.5}O_4$ cathode and $Li_{10}GeP_2S_{12}$ solid electrolyte, Chem. Mater. 28 (2016) 2634–2640, https://doi.org/10.1021/acs.chemmater.5b04940.
[38] H. Kwak, S. Wang, J. Park, Y. Liu, K.T. Kim, Y. Choi, Y. Mo, Y.S. Jung, Emerging halide superionic conductors for all-solid-state batteries: design, synthesis, and practical applications, ACS Energy Lett. 7 (2022) 1776–1805, https://doi.org/10.1021/acsenergylett.2c00438.
[39] X. Li, J. Liang, J. Luo, M. Norouzi Banis, C. Wang, W. Li, S. Deng, C. Yu, F. Zhao, Y. Hu;, et al., Air-stable Li_3InCl_6 electrolyte with high voltage compatibility for all-solid-state batteries, Energy Environ. Sci. 12 (2019) 2665–2671, https://doi.org/10.1039/c9ee02311a.
[40] J. Liang, X. Li, S. Wang, K.R. Adair, W. Li, Y. Zhao, C. Wang, Y. Hu, L. Zhang, S. Zhao;, et al., Site-occupation-tuned superionic Li_xScCl_{3+x} halide solid electrolytes for all-solid-state batteries, J. Am. Chem. Soc. 142 (2020) 7012–7022, https://doi.org/10.1021/jacs.0c00134.
[41] L. Zhou, C.Y. Kwok, A. Shyamsunder, Q. Zhang, X. Wu, L.F. Nazar, A new halospinel superionic conductor for high-voltage all solid state lithium batteries, Energy Environ. Sci. 13 (2020) 2056–2063, https://doi.org/10.1039/d0ee01017k.
[42] Z. Liu, S. Ma, J. Liu, S. Xiong, Y. Ma, H. Chen, High ionic conductivity achieved in $Li_3Y(Br_3Cl_3)$ mixed halide solid electrolyte via promoted diffusion pathways and enhanced grain boundary, ACS Energy Lett. 6 (2020) 298–304, https://doi.org/10.1021/acsenergylett.0c01690.
[43] H. Kwak, D. Han, J. Lyoo, J. Park, S.H. Jung, Y. Han, G. Kwon, H. Kim, S.T. Hong, K.W. Nam;, et al., New cost-effective halide solid electrolytes for all-solid-state batteries: mechanochemically prepared Fe^{3+}-substituted Li_2ZrCl_6, Adv. Energy Mater. 11 (2021), 2003190, https://doi.org/10.1002/aenm.202003190.
[44] J. Park, D. Han, H. Kwak, Y. Han, Y.J. Choi, K.-W. Nam, Y.S. Jung, Heat treatment protocol for modulating ionic conductivity via structural evolution of $Li_{3-x}Yb_{1-x}M_xCl_6$ (M = Hf^{4+}, Zr^{4+}) new halide superionic conductors for all-solid-state batteries, Chem. Eng. J. 425 (2021), 130630, https://doi.org/10.1016/j.cej.2021.130630.
[45] H. Kwak, D. Han, J.P. Son, J.S. Kim, J. Park, K.-W. Nam, H. Kim, Y.S. Jung, Li^+ conduction in aliovalent-substituted monoclinic Li_2ZrCl_6 for all-solid-state batteries: $Li_{2+x}Zr_{1-x}M_xCl_6$ (M = In, Sc), Chem. Eng. J. 437 (2022), 135413, https://doi.org/10.1016/j.cej.2022.135413.
[46] J. Park, J.P. Son, W. Ko, J.-S. Kim, Y. Choi, H. Kim, H. Kwak, D.-H. Seo, J. Kim, Y. S. Jung, $NaAlCl_4$: new halide solid electrolyte for 3 v stable cost-effective all-solid-state na-ion batteries, ACS Energy Lett. 7 (2022) 3293–3301, https://doi.org/10.1021/acsenergylett.2c01514.
[47] S. Wang, Q. Bai, A.M. Nolan, Y. Liu, S. Gong, Q. Sun, Y. Mo, Lithium chlorides and bromides as promising solid-state chemistries for fast ion conductors with good electrochemical stability, Angew. Chem. Int. Ed. 58 (2019) 8039–8043, https://doi.org/10.1002/anie.201901938.
[48] K.-H. Park, K. Kaup, A. Assoud, Q. Zhang, X. Wu, L.F. Nazar, High-voltage superionic halide solid electrolytes for all-solid-state Li-Ion batteries, ACS Energy Lett. 5 (2020) 533–539, https://doi.org/10.1021/acsenergylett.9b02599.
[49] H. Kwak, J. Lyoo, J. Park, Y. Han, R. Asakura, A. Remhof, C. Battaglia, H. Kim, S.-T. Hong, Y.S. Jung, Na_2ZrCl_6 enabling highly stable 3 V all-solid-state Na-ion batteries, Energy Storage Mater. 37 (2021) 47–54, https://doi.org/10.1016/j.ensm.2021.01.026.
[50] S.H. Jung, D.H. Kim, P. Brüner, H. Lee, H.J. Hah, S.K. Kim, Y.S. Jung, Extremely conductive RuO_2-coated $LiNi_{0.5}Mn_{1.5}O_4$ for lithium-ion batteries, Electrochim. Acta 232 (2017) 236–243, https://doi.org/10.1016/j.electacta.2017.02.109.
[51] C. Zhu, R.E. Usiskin, Y. Yu, J. Maier, The nanoscale circuitry of battery electrodes, Science 358 (2017) 1400, https://doi.org/10.1126/science.aao2808.
[52] A.L. Davis, V. Goel, D.W. Liao, M.N. Main, E. Kazyak, J. Lee, K. Thornton, N. P. Dasgupta, Rate limitations in composite solid-state battery electrodes: revealing heterogeneity with operando microscopy, ACS Energy Lett. 6 (2021) 2993–3003, https://doi.org/10.1021/acsenergylett.1c01063.
[53] Y.J. Nam, D.Y. Oh, S.H. Jung, Y.S. Jung, Toward practical all-solid-state lithium-ion batteries with high energy density and safety: comparative study for electrodes fabricated by dry- and slurry-mixing processes, J. Power Sources 375 (2018) 93–101, https://doi.org/10.1016/j.jpowsour.2017.11.031.
[54] C. Sangrós Giménez, L. Helmers, C. Schilde, A. Diener, A. Kwade, Modeling the electrical conductive paths within all-solid-state battery electrodes, Chem. Eng. Technol. 43 (2020) 819–829, https://doi.org/10.1002/ceat.201900501.
[55] C. Park, S. Lee, K. Kim, M. Kim, S. Choi, D. Shin, Electrochemical properties of composite cathode using bimodal sized electrolyte for all-solid-state batteries, J. Electrochem. Soc. 166 (2019) A5318–A5322, https://doi.org/10.1149/2.0481903jes.
[56] T. Shi, Q. Tu, Y. Tian, Y. Xiao, L.J. Miara, O. Kononova, G. Ceder, High active material loading in all-solid-state battery electrode via particle size optimization, Adv. Energy Mater. 10 (2019), 1902881, https://doi.org/10.1002/aenm.201902881.
[57] E. Ayerbe, M. Berecibar, S. Clark, A.A. Franco, J. Ruhland, Digitalization of battery manufacturing: current status, challenges, and opportunities, Adv. Energy Mater. 12 (2021), 2102696, https://doi.org/10.1002/aenm.202102696.
[58] J. Park, K.T. Kim, D.Y. Oh, D. Jin, D. Kim, Y.S. Jung, Y.M. Lee, Digital twin-driven all-solid-state battery: unraveling the physical and electrochemical behaviors, Adv. Energy Mater. 10 (2020), 2001563, https://doi.org/10.1002/aenm.202001563.
[59] A. Bielefeld, D.A. Weber, J. Janek, Modeling effective ionic conductivity and binder influence in composite cathodes for all-solid-state batteries, ACS Appl. Mater. Interfaces 12 (2020) 12821–12833, https://doi.org/10.1021/acsami.9b22788.
[60] M. So, G. Inoue, K. Park, K. Nunoshita, S. Ishikawa, Y. Tsuge, Simulation of the compaction of an all-solid-state battery cathode with coated particles using the

discrete element method, J. Power Sources 530 (2022), https://doi.org/10.1016/j.jpowsour.2022.231279.
[61] K.T. Kim, D.Y. Oh, S. Jun, Y.B. Song, T.Y. Kwon, Y. Han, Y.S. Jung, Tailoring slurries using cosolvents and li salt targeting practical all-solid-state batteries employing sulfide solid electrolytes, Adv. Energy Mater. 11 (2021), https://doi.org/10.1002/aenm.202003766.
[62] K. Märker, P.J. Reeves, C. Xu, K.J. Griffith, C.P. Grey, Evolution of structure and lithium dynamics in $LiNi_{0.8}Mn_{0.1}Co_{0.1}O_2$ (NMC811) cathodes during electrochemical cycling, Chem. Mater. 31 (2019) 2545–2554, https://doi.org/10.1021/acs.chemmater.9b00140.
[63] D.Y. Oh, Y.J. Nam, K.H. Park, S.H. Jung, K.T. Kim, A.R. Ha, Y.S. Jung, Slurry-fabricable Li^+-conductive polymeric binders for practical all-solid-state lithium-ion batteries enabled by solvate ionic liquids, Adv. Energy Mater. 9 (2019), 1802927, https://doi.org/10.1002/aenm.201802927.
[64] J. Li, R. Shunmugasundaram, R. Doig, J.R. Dahn, *In situ* X-ray diffraction study of layered Li–Ni–Mn–Co oxides: effect of particle size and structural stability of core–shell materials, Chem. Mater. 28 (2015) 162–171, https://doi.org/10.1021/acs.chemmater.5b03500.
[65] T. Hakari, M. Deguchi, K. Mitsuhara, T. Ohta, K. Saito, Y. Orikasa, Y. Uchimoto, Y. Kowada, A. Hayashi, M. Tatsumisago, Structural and electronic-state changes of a sulfide solid electrolyte during the Li deinsertion–insertion processes, Chem. Mater. 29 (2017) 4768–4774, https://doi.org/10.1021/acs.chemmater.7b00551.
[66] T. Koç, F. Marchini, G. Rousse, R. Dugas, J.-M. Tarascon, In search of the best solid electrolyte-layered oxide pairing for assembling practical all-solid-state batteries, ACS Applied Energy Materials 4 (2021) 13575–13585, https://doi.org/10.1021/acsaem.1c02187.
[67] A. Banerjee, H. Tang, X. Wang, J.H. Cheng, H. Nguyen, M. Zhang, D.H.S. Tan, T. A. Wynn, E.A. Wu, J.M. Doux;, et al., Revealing nanoscale solid-solid interfacial phenomena for long-life and high-energy all-solid-state batteries, ACS Appl. Mater. Interfaces 11 (2019) 43138–43145, https://doi.org/10.1021/acsami.9b13955.
[68] W. Zhang, T. Leichtweiss, S.P. Culver, R. Koerver, D. Das, D.A. Weber, W.G. Zeier, J. Janek, The detrimental effects of carbon additives in Li10GeP2S12-based solid-state batteries, ACS Appl. Mater. Interfaces 9 (2017) 35888–35896, https://doi.org/10.1021/acsami.7b11530.
[69] S. Deng, Y. Sun, X. Li, Z. Ren, J. Liang, K. Doyle-Davis, J. Liang, W. Li, M. Norouzi Banis, Q. Sun;, et al., Eliminating the detrimental effects of conductive agents in sulfide-based solid-state batteries, ACS Energy Lett. 5 (2020) 1243–1251, https://doi.org/10.1021/acsenergylett.0c00256.
[70] S. Randau, F. Walther, A. Neumann, Y. Schneider, R.S. Negi, B. Mogwitz, J. Sann, K. Becker-Steinberger, T. Danner, S. Hein;, et al., On the additive microstructure in composite cathodes and alumina-coated carbon microwires for improved all-solid-state batteries, Chem. Mater. 33 (2021) 1380–1393, https://doi.org/10.1021/acs.chemmater.0c04454.